

## Oxygen defects in GaAs: A hybrid functional study

Davide Colleoni and Alfredo Pasquarello

*Chaire de Simulation à l'Echelle Atomique (CSEA), Ecole Polytechnique Fédérale de Lausanne (EPFL), CH-1015 Lausanne, Switzerland*

(Received 3 September 2015; revised manuscript received 24 February 2016; published 15 March 2016)

Using hybrid density functional calculations, we address the structural properties, formation energies, and charge transition levels of a variety of oxygen defects in GaAs. The set of considered defects comprises the bridging O atom in a As-O-Ga configuration, interstitial O atoms in tetrahedral sites, and O atoms substitutional to either Ga ( $O_{\text{Ga}}$ ) or As atoms ( $O_{\text{As}}$ ). In addition, we consider an As vacancy containing two O atoms, for which the most stable configurations are found through the use of molecular dynamics simulations, and defect complexes involving a  $O_{\text{As}}$  defect bound to either one or two  $\text{As}_{\text{Ga}}$  antisites, denoted  $\text{As}_{\text{Ga}}\text{-}O_{\text{As}}$  and  $(\text{As}_{\text{Ga}})_2\text{-}O_{\text{As}}$ , respectively. We find that the bridging O defect and the  $\text{As}_{\text{Ga}}\text{-}O_{\text{As}}$  and  $(\text{As}_{\text{Ga}})_2\text{-}O_{\text{As}}$  complexes are the most stable oxygen defects in GaAs. The actual occurrence of these defects is examined against two criteria. The first criterion concerns the stability against O dissociation and is evaluated via the calculation of dissociation energies. The second criterion involves the defect formation at thermodynamic equilibrium and is inferred from the comparison between the formation energy of the oxygen defect and that of its O-related dissociation product (bridging O defect). Both the  $\text{As}_{\text{Ga}}\text{-}O_{\text{As}}$  and  $(\text{As}_{\text{Ga}})_2\text{-}O_{\text{As}}$  complexes satisfy these criteria and are stable against O dissociation. Further analysis in cooled-down conditions leads us to dismiss the  $\text{As}_{\text{Ga}}\text{-}O_{\text{As}}$  defect due to the more favorable bonding of two rather than one  $\text{As}_{\text{Ga}}$  antisites. The conclusion that only the bridging O defect and the  $(\text{As}_{\text{Ga}})_2\text{-}O_{\text{As}}$  complex are expected to occur is in accord with experimental observations.

DOI: [10.1103/PhysRevB.93.125208](https://doi.org/10.1103/PhysRevB.93.125208)

### I. INTRODUCTION

GaAs is the prototype III-V semiconductor material and has found successful applications in optoelectronic devices [1]. More recently, a revived interest has aroused in GaAs as replacement to silicon in future metal-oxide-semiconductor field-effect transistors [2,3]. However, its widespread use for such a technological application is hampered by the high concentration of defect states at its interfaces with typical oxides [4,5]. In several cases, Fermi-level pinning has been observed and related to the presence of defects [4,6–19].

Oxygen is the most common unintentional impurity in GaAs and can be present in concentrations ranging between  $10^{14}$  and  $10^{20}$   $\text{cm}^{-3}$ , depending on growth technique [20,21]. Local vibrational mode (LVM) spectroscopy has been largely used to experimentally investigate oxygen defects in GaAs [22–26]. The absorption peak at  $845$   $\text{cm}^{-1}$  is associated to an interstitial oxygen atom which is bridging a Ga and an As atom ( $O_{\text{b}}$ ) [27,28]. This bridging configuration appears to be electrically inactive [29,30]. The LVM spectra show three other oxygen-related absorption bands, located at  $730.7$ ,  $714.9$ , and  $714.2$   $\text{cm}^{-1}$  and labeled A, B, and B' [27,31,32]. These lines show a triplet fine structure due to the Ga isotopic concentration and have thus clearly been associated to a Ga-O-Ga structure [27]. The three LVM lines refer to different charge states of the same defect [31,32] which is shown to be electrically active [20] and to give Fermi-level pinning at  $0.36\text{--}0.43$  eV below the conduction band minimum (CBM) [13,33]. Moreover, the charge state associated to the B' line is found to be paramagnetic [34], metastable [29,31,32], and to correspond to the neutral charge state [35]. The A and B lines correspond to the +1 and –1 charge states, respectively [33].

The identification of the nature of the underlying defects strongly relies on density functional calculations. Most of the available calculations are based on semilocal density functionals. Early calculations supported a  $V_{\text{As}}\text{-}O$  defect structure

as candidate for the Ga-O-Ga defect [36–38], proposed in analogy to the VO center in silicon [27]. Later, Taguchi and Kageshima proposed an interstitial configuration in which the O atom binds to only two Ga atoms [39]. However, neither of these calculations could fully account for the stable charge states identified experimentally. Pesola *et al.* then proposed a defect complex, denoted  $(\text{As}_{\text{Ga}})_2\text{-}O_{\text{As}}$  defect, in which the  $O_{\text{As}}$  defect shows two  $\text{As}_{\text{Ga}}$  antisites in its first-neighbor shell [40]. This defect model shows good agreement with experiment as far as the vibrational frequencies and the involved charge states are concerned, but produces a charge transition level at mid-gap [40], which is inconsistent with the energy at which the Fermi level is pinned [20].

Recent years have witnessed important advances in the theoretical study of point defects [41,42]. The most significant one is the systematic use of hybrid density functionals which open the band gaps of the host materials bringing them closer to their experimental values. Hybrid functionals have been shown to lead to agreement within  $0.2$  eV for the defect levels of the As antisite in GaAs [43]. Additionally, a robust framework has been developed for the treatment of finite-size effects associated to charged defect states subject to periodic boundary conditions [44,45]. In particular, clear criteria have been proposed to eliminate spurious defect charge states, in which the charge is not localized at the defect site [45]. Recently, these methodological advances have been applied to specific oxygen defects in GaAs. Through the use of hybrid functional calculations, the  $O_{\text{As}}$  defect was unambiguously ruled out as a candidate for the Ga-O-Ga defect [46]. Furthermore, reconsideration of the  $(\text{As}_{\text{Ga}})_2\text{-}O_{\text{As}}$  defect led to energies for Fermi-level pinning and optical transitions between defect charge states in very good agreement with experiment [47]. These calculations clearly offer a new perspective on the description of oxygen defects in GaAs and call for a comprehensive study of these defects through the use of state-of-the-art methodologies.

In this work, we set out to determine accurate formation energies and charge transition levels for a large set of oxygen defects in GaAs using hybrid functional calculations. Our study includes O impurities in various interstitial and substitutional sites. In particular, we investigate the case of an As vacancy containing two O atoms using molecular dynamics techniques to identify its stable structure. We also consider defect complexes such as  $\text{As}_{\text{Ga}}\text{-O}_{\text{As}}$  and  $(\text{As}_{\text{Ga}})_2\text{-O}_{\text{As}}$  defects, in which the  $\text{O}_{\text{As}}$  defect binds to either one or two  $\text{As}_{\text{Ga}}$  antisites. We then examine the stability of the most stable oxygen defects against the dissociation of O or As antisites.

The formation energies and the charge transition levels of the  $\text{O}_{\text{As}}$  and  $(\text{As}_{\text{Ga}})_2\text{-O}_{\text{As}}$  defects have been the object of previous communications and are here only briefly summarized for completeness [46,47]. However, these defects are here considered in the global comparison of the energetics and in the study of the dissociation into smaller defect units.

The paper is organized as follows. In Sec. II, we describe the adopted theoretical approach. Our computational scheme is first detailed and then validated through a series of convergence checks. The energetics of the considered defects are discussed individually in Sec. III. In Sec. IV, the  $\text{As}_{\text{Ga}}\text{-O}_{\text{As}}$  and  $(\text{As}_{\text{Ga}})_2\text{-O}_{\text{As}}$  complexes, which count among the most stable defects, are examined against dissociation of oxygen and of As antisites. In Sec. V, the formation energies of the various defects are compared and the conclusions are drawn.

## II. THEORETICAL APPROACH

### A. Defect formation energy

In this work, we calculate defect formation energies and thermodynamic charge transition levels. The latter correspond to Fermi energies at which the formation energies of competing charge states are equal. The formation energy  $E_f(X^q)$  is a function of Fermi energy ( $\epsilon_F$ ) given with respect to the valence band maximum (VBM), according to [48]

$$E_f(X^q) = E_{\text{tot}}[X^q] + E_{\text{corr}}^q - E_{\text{tot}}[\text{bulk}] - \sum_i n_i \mu_i + q(\epsilon_F + \epsilon_v + \Delta v_{0/b}), \quad (1)$$

where  $E_{\text{tot}}[X^q]$  is the total energy of the supercell containing the charged defect  $X^q$  and  $E_{\text{tot}}[\text{bulk}]$  the total energy of the pristine bulk supercell. For each species  $i$ , the chemical potential  $\mu_i$  of the  $n_i$  added/removed atoms allows us to describe various experimental conditions.  $\epsilon_v$  corresponds to the VBM of GaAs as obtained from a separate bulk calculation.  $\Delta v_{0/b}$  is a potential alignment term which accounts for the potential shift between the bulk and the neutral defect calculation [45,48]. Finally,  $E_{\text{corr}}^q$  corrects for the finite-size error due to the long-range nature of the Coulomb interaction and the use of periodic boundary conditions.

In this work, we correct our results through the scheme proposed by Freysoldt, Neugebauer, and Van de Walle [44]. This scheme also allows one to control the defect charge localization by studying the planar average of the electrostatic potential far from the defect and checking whether it tends to a constant value [44,46]. When the defect state is localized within the supercell, the planar average of the electrostatic potential is well reproduced by that of a model Gaussian charge

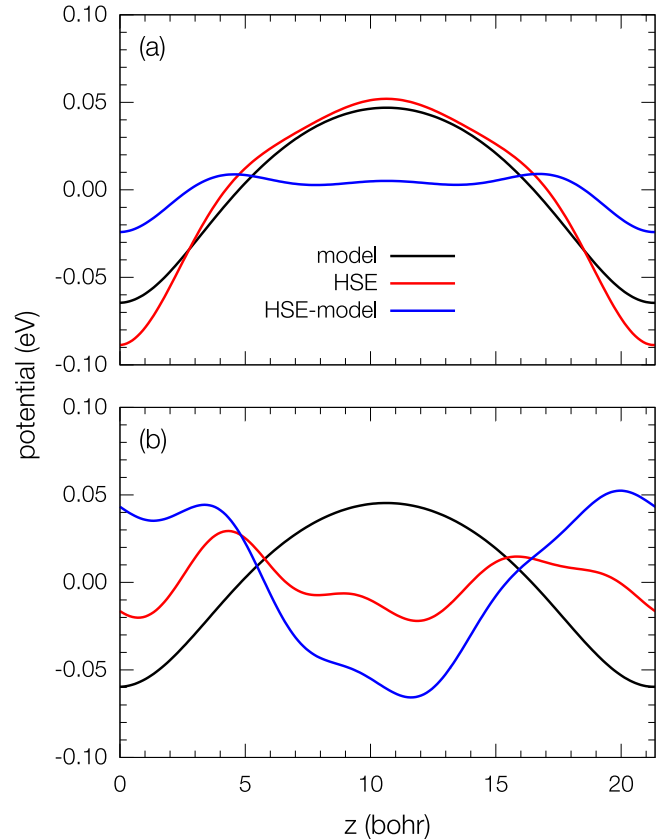


FIG. 1. Planar averages of the electrostatic potential of (a) the  $\text{O}_{\text{As}}$  defect (Sec. III A) and of (b) the  $\text{O}_i\text{-Ga}_4$  defect (Sec. III B), both in the charge state  $-1$ , as obtained with the Heyd-Scuseria-Ernzerhof (HSE) functional (red). The defect is located at the origin. The black lines correspond to the potential of a model Gaussian charge distribution with a width of 1 bohr (model). The blue lines represent the short-range defect potential and are obtained from the difference between the red and the black lines.

distribution, as shown in Fig. 1(a). The short-range potential is obtained as the difference between the model potential and the potential resulting from the electronic structure calculation. This short-range potential shows a flat behavior far away from the defect site [44]. For illustration, we show in Fig. 1(b) a case in which the defect charge is not well localized. In this case, the difference between the electronic structure and model potentials is no longer short range and strongly oscillates far from the defect site. In some cases, these electrostatic considerations might not be sufficient to determine whether the defect state is well localized within the adopted supercell. The calculation of the screening charge is then a better indicator for the defect charge localization [45].

### B. Computational setup

All defect structures are obtained through full structural relaxation carried out within a density functional theory framework in which the exchange-correlation energy is described through the semilocal approximation proposed by Perdew, Burke, and Ernzerhof (PBE) [49]. We use plane-wave basis sets defined by a kinetic energy cutoff of 70 Ry together

with norm-conserving pseudopotentials as implemented in the QUANTUM ESPRESSO suite of programs [50].

Troullier-Martins-type pseudopotentials generated with the FHI98PPcode are used in this work [51,52]. The pseudopotentials are generated within the PBE scheme. Only  $s$  and  $p$  valence states are explicitly considered for Ga, As, and O. The maximum angular momentum component is three for Ga and As and two for O. We take the local potential in the  $s$  wave for Ga, and in the  $d$  wave for As and O. To validate the present pseudopotentials, we calculate with PBE a set of equilibrium properties for bulk GaAs and for atomic and molecular oxygen.

For bulk GaAs, we use a two-atom primitive supercell, a cutoff of 70 Ry, and a  $12 \times 12 \times 12$   $\mathbf{k}$ -point mesh and vary the lattice parameter between 5.625 and 5.875 Å. We fit the total energy as a function of the lattice parameter using a Murnaghan equation [53]. The resulting equilibrium lattice parameter ( $a_0$ ), bulk modulus, and its pressure derivative compare well with previous generalized-gradient results [54,55] and experimental data [56,57] as shown in Table I. We also calculate the cohesive energy and find it to be close to previous theoretical [54,55] and experimental results [56]. The formation enthalpy also agrees well with its experimental counterpart [58] (cf. Table I). Using the PBE lattice parameter, we obtain a band gap of 0.24 eV, close to previous estimates [43,62].

For atomic oxygen, we use a cubic box with a side of 11 Å and a  $\mathbf{k}$ -point sampling consisting of the sole  $\Gamma$  point. The first ionization energy (IE) and the electron affinity (EA) compare very well with their experimental counterparts [59,60], as shown in Table I. The calculated bond length and binding

TABLE I. Equilibrium lattice parameter ( $a_0$ ), bulk modulus ( $B_0$ ) and its pressure derivative ( $B'_0$ ), cohesive energy ( $E_c$ ), and formation enthalpy ( $\Delta H$ ) for crystalline GaAs. First ionization energy (IE) and electron affinity (EA) for atomic O. Bond length and binding energy for  $O_2$ . All results are obtained with the PBE functional. We compare the present values for GaAs with generalized-gradient results in Refs. [54,55]. Experimental values taken from Refs. [56–58] are also shown. Experimental values for the IE and AE of atomic oxygen and for the equilibrium bond length ( $R_0$ ) and binding energy ( $E_b$ ) of molecular oxygen are taken from Refs. [59–61].

GaAs	$a_0$ (Å)	$B_0$ (kbar)	$B'_0$	$-E_c$ (eV)	$\Delta H$ (eV)
This work	5.75	595	4.76	6.11	0.71
Ref. [54]	5.72	621		6.36	
Ref. [55]	5.76	660	3.63	6.49	
Expt.	5.65 <sup>a</sup>	756 <sup>a</sup>	4.56 <sup>b</sup>	6.52 <sup>a</sup>	0.74 <sup>c</sup>
O		IE (eV)		EA (eV)	
This work		13.87		1.57	
Expt.		13.62 <sup>d</sup>		1.46 <sup>e</sup>	
$O_2$		$R_0$ (Å)		$E_b$ (eV)	
This work		1.215		5.91	
Expt.		1.207 <sup>f</sup>		5.12 <sup>f</sup>	

<sup>a</sup>Reference [56].

<sup>b</sup>Reference [57].

<sup>c</sup>Reference [58].

<sup>d</sup>Reference [59].

<sup>e</sup>Reference [60].

<sup>f</sup>Reference [61].

energy of molecular  $O_2$  is also found in good agreement with the experimental values [61].

In this work, the defects are generally studied in 64-atom supercells. For particular purposes, we carry out a few calculations using larger supercells containing 216 and 512 atoms. For the relaxed structures, the electronic structure is finally obtained through the use of the hybrid functional proposed by Heyd, Scuseria, and Ernzerhof (HSE) [63,64]. This functional is implemented in the QUANTUM ESPRESSO suite of programs as described in Ref. [65]. We adopt the original range-separation parameter ( $\mu = 0.11$  bohr<sup>-1</sup>, Ref. [63]) to preserve the overall accuracy of the functional [65]. However, we set the fraction of nonlocal Fock exchange to  $\alpha = 0.35$  in order to reproduce the experimental band gap of GaAs ( $E_g = 1.52$  eV, Ref. [66]), following the scheme described in Ref. [43]. The structural properties generally depend very weakly on  $\alpha$ , while the band gap increases linearly with  $\alpha$  [65]. The nonlocal exchange potential is treated as described in Ref. [67]. In these calculations, pseudopotentials generated with the PBE functional are used [67–69]. We carry out spin-polarized calculations. Various spin states are taken under consideration within PBE. In the case of an even number of electrons, the calculation with an equal number of electrons in the two spin states leads to the most stable result. In the case of an odd number of electrons, the most stable state corresponds to the case in which the number of electrons in the two spin states differs by one. The final HSE calculations are only performed for the most stable spin states found with PBE.

The size of our supercells is based on the experimental lattice parameter of 5.65 Å (Ref. [66]). We prefer using the experimental lattice constant rather than the PBE equilibrium value (5.75 Å), as our final calculations are performed at the HSE level which yields an equilibrium lattice parameter (5.68 Å) differing by less than 0.5% from the experimental value [43]. This choice does not affect the calculated charge transition levels in any significant way [43].

The use of hybrid functionals is motivated by the necessity of opening the band gap [42] in order to achieve proper localization of the defect states [45]. Indeed, at the experimental lattice parameter the band gap of GaAs calculated with PBE is particularly small (0.67 eV), favoring spurious hybridization effects between the localized defect states and the delocalized bands of the host [45].

The use of hybrid functionals for structural relaxations involves a high computational cost and would limit the number of defects that could be studied in this work. We therefore resort to the following relaxation scheme based on the use of the PBE functional. For 64-atom supercells, we use an off-center  $2 \times 2 \times 2$   $\mathbf{k}$ -point mesh, which does not include the  $\Gamma$  point. Within PBE, this  $\mathbf{k}$ -point sampling gives defect formation energies and defect levels converged to 0.2 and 0.15 eV, respectively, as shown in Sec. II C. This sampling additionally offers the advantage of opening the band gap in a similar way as the HSE functional (cf. Fig. 2), when the band structures are aligned with respect to the electrostatic potential. With this alignment, energy levels of atomically localized defects remain approximately constant when going from PBE to HSE calculations [42,65,70,71]. As can be seen in Fig. 2, the band gap achieved through the PBE calculation with an off-center  $\mathbf{k}$ -point mesh spans almost the entirety of the

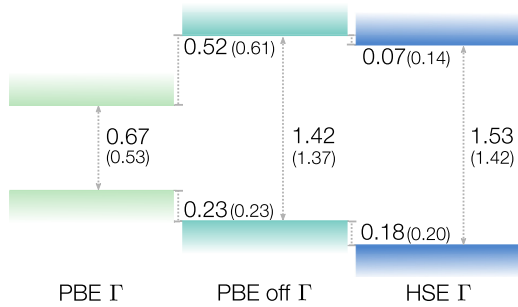


FIG. 2. Calculated band gaps of GaAs as obtained at the PBE (PBE  $\Gamma$ ) and HSE levels (HSE  $\Gamma$ ) with  $\mathbf{k}$ -point samplings including the  $\Gamma$  point. The middle panel corresponds to a PBE calculation with an off-center  $2 \times 2 \times 2$   $\mathbf{k}$ -point mesh (PBE off  $\Gamma$ ). The band structures are aligned through the average electrostatic potential [42,70,71]. Band gaps and band offsets are in eV. The valence band in the HSE representation has been shifted upwards by 0.1 eV to account for spin-orbit effects, as suggested in Ref. [43]. Values in parentheses refer to calculations in which the lattice parameter is fixed at the HSE equilibrium value of 5.68 Å (Ref. [43]).

HSE band gap giving access to defect states in a wide energy range. A small energy region in the vicinity of the valence band remains inaccessible through this approach, but an *a posteriori* check shows that none of the defect levels obtained in this work are concerned. Such a PBE scheme ensures a proper description of the charge localization during the structural relaxation. For higher accuracy, the final electronic properties of our 64-atom supercells are obtained through a HSE calculation with a  $2 \times 2 \times 2$   $\mathbf{k}$  mesh including the  $\Gamma$  point [43,72].

The present scheme therefore does not yield relaxed model structures at the hybrid functional level. Nevertheless, such relaxations generally only yield minor structural changes, as found in a benchmark study on the  $\text{As}_{\text{Ga}}$  antisite [43]. In Sec. II C, a detailed study on a representative O defect confirms that converged results can be achieved without performing structural relaxations at the hybrid-functional level. More generally, for particular defects, hybrid functionals may lead to asymmetric relaxations leading to more localized defect states, due to a better cancellation of the self-interaction [73–76]. However, even in these cases, the defect energies are generally only marginally affected, as the asymmetric structure arises from a subtle competition between the delocalized and the localized state [75].

In this work, we adopt the As-rich condition, which is the standard growth condition of GaAs for electronic applications [77,78]. We obtain the As chemical potential  $\mu_{\text{As}}$  from the tetrahedral  $\text{As}_4$  molecule, as it is the molecular precursor adopted in the molecular beam epitaxy of GaAs [79]. With HSE [63], this reference is 0.22 eV less stable than the tetragonal phase of crystalline As. This value corresponds to the PBE-optimized lattice structure of the minimal tetragonal cell of solid As, for which we obtain lattice parameters of  $a = 3.85$  and  $c = 10.64$  Å in good agreement with experimental values of  $a = 3.76$  and  $c = 10.55$  Å (Ref. [80]). The chemical potential of Ga,  $\mu_{\text{Ga}}$ , is then derived from the equilibrium condition with GaAs,  $\mu_{\text{Ga}} = \mu_{\text{GaAs}} - \mu_{\text{As}}$ . The O chemical potential  $\mu_{\text{O}}$  is derived from the equilibrium condition with

$\beta\text{-Ga}_2\text{O}_3$ , as the occurrence of Ga oxides is observed during oxidation [81]. Through PBE calculations, we obtain for  $\beta\text{-Ga}_2\text{O}_3$  lattice parameters of  $a = 12.26$ ,  $b = 3.07$ , and  $c = 5.82$  Å, to be compared with the corresponding experimental values of  $a = 12.23$ ,  $b = 3.04$ , and  $c = 5.80$  Å (Ref. [82]). The presently adopted chemical potential for O is lower by 3.05 eV than that derived from molecular oxygen.

### C. Convergence checks

As far as the accuracy of hybrid functional calculations, a benchmark calculation involving the  $\text{As}_{\text{Ga}}$  antisite has shown that calculated charge transition levels can be expected to agree with their experimental counterparts within  $\sim 0.2$  eV [43]. This accuracy thus sets the scale for the convergence of our calculations. To demonstrate that the present computational setup yields converged results, we here perform several tests considering the most stable O defects identified in this work. In particular, we consider the explicit treatment of Ga  $3d$  electrons, the use of larger supercells and denser  $\mathbf{k}$ -point meshes, and the effect of structural relaxation at the hybrid functional level.

To estimate the effect of explicitly considering the Ga  $3d$  electrons, we perform PBE calculations with norm-conserving pseudopotentials generated with or without Ga  $3d$  states included in the valence. We focus on the formation energies and energy levels of the  $(\text{As}_{\text{Ga}})_2\text{-O}_{\text{As}}$  defect. This is the most stable defect found in this work. This defect also has the largest size, as it extends over three atomic sites (*vide infra*). The Ga pseudopotential including the  $3d$  states is generated through the Troullier-Martins scheme [51]. The defect calculation is performed in a 64-atom supercell using a  $2 \times 2 \times 2$  off- $\Gamma$   $\mathbf{k}$ -point mesh and an energy cutoff of 90 Ry. As can be seen in Table II, the results obtained with the explicit treatment of the  $3d$  electrons compare well with those achieved using a Ga pseudopotential without  $3d$  states in the valence. The charge transition levels are affected by less than 0.1 eV and the defect formation energies by less than 0.3 eV. A similar study on the  $\text{As}_{\text{Ga}}$  defect in Ref. [43] yielded similar conclusions. The corresponding results have been added to

TABLE II. Charge transition levels ( $\varepsilon_{q/q'}$ ) and formation energies ( $E_f$ ) calculated at the PBE level with and without Ga  $3d$  states in the valence, for the most stable O defect identified in this work ( $(\text{As}_{\text{Ga}})_2\text{-O}_{\text{As}}$ ). An off- $\Gamma$   $2 \times 2 \times 2$   $\mathbf{k}$ -point mesh is used. For comparison, we also show corresponding energies for the As antisite from Refs. [43,83]. Energies are given in eV.

	Without Ga $3d$	With Ga $3d$
$(\text{As}_{\text{Ga}})_2\text{-O}_{\text{As}}$		
$\varepsilon_{+1/-1}$	0.93	0.84
$E_f(q = +1)$	1.15	1.05
$E_f(q = -1)$	3.00	2.72
$\text{As}_{\text{Ga}}$		
$\varepsilon_{+2/+1}$	0.35	0.25
$\varepsilon_{+1/0}$	0.78	0.65
$E_f(q = +2)$	0.01	0.43
$E_f(q = +1)$	0.36	0.68
$E_f(q = 0)$	1.14	1.33

Table II for completeness. Therefore, we estimate that the explicit treatment of the Ga  $3d$  electrons might affect the calculated charge transition levels by  $\sim 0.1$  eV and the absolute formation energies by  $\sim 0.3$  eV. Given the expected accuracy of  $\sim 0.2$  eV for defect levels [43], we do not explicitly retain Ga  $3d$  electrons in our study. We do not include partial core corrections, as they do not lead to any clear improvement of the bulk equilibrium properties of GaAs [54].

Next, we investigate the cell size and  $\mathbf{k}$ -point density required for achieving converged defect energies. As we aim at using hybrid functionals, these tests are particularly important to minimize the overall computational cost. We performed extensive tests with PBE. We calculate formation energies and charge transition levels for a series of defects, including the four most stable O defects and their parent unoxidized defects. To check the convergence, we consider two different supercell sizes containing 64 and 216 atoms. We systematically use the same  $2 \times 2 \times 2$   $\mathbf{k}$ -point mesh, thereby implying a higher  $\mathbf{k}$ -point density in the calculation with the larger cell. The  $\mathbf{k}$ -point mesh is shifted to avoid the  $\Gamma$  point, as recommended in the literature [84]. Our results are given in Tables III and IV. Despite the large size of some of the considered defects, their electronic properties are already well described with the 64-atom supercell. Indeed, the defect formation energies obtained with this cell size differ by less than 0.2 eV from those obtained with the 216-atom supercells provided the finite-size correction is applied (Table III). The same conclusion also applies to the charge transition levels, for which the largest difference of 0.15 eV is found for the  $O_{As}$  defect. Hence, this comparison shows that 64-atom supercells with a  $2 \times 2 \times 2$

TABLE III. Formation energies [ $E_f(X^q)$ ] and their finite-size corrections ( $E_{\text{corr}}^q$ ) for a series of relevant defects, including the most stable O defects and their dissociation products, as calculated at the PBE level of theory with 64-atom and 216-atom supercells and a  $2 \times 2 \times 2$   $\mathbf{k}$ -point mesh. Various stable charge states  $q$  are considered. The last column gives the difference  $\Delta E_f(X^q)$  between the formation energies obtained with the two supercell sizes. The Fermi level is taken at the VBM ( $p$ -type condition) obtained in a HSE calculation and aligned through the average electrostatic potential. Energies are given in eV.

Defect	$q$	64-atom		216-atom		$\Delta E_f(X^q)$
		$E_f(X^q)$	$E_{\text{corr}}^q$	$E_f(X^q)$	$E_{\text{corr}}^q$	
$V_{Ga}/V_{As}-As_{Ga}$	+3	1.84	1.40	1.88	1.05	0.04
	-2	3.00	0.70	3.03	0.41	0.03
	-3	3.99	1.37	3.90	0.85	0.09
$V_{As}-2As_{Ga}/V_{Ga}-As_{Ga}$	+1	0.89	0.11	0.79	0.08	0.10
	-1	1.98	0.11	2.03	0.08	0.05
	-2	3.16	0.46	3.25	0.31	0.09
$O_b$	0	2.40		2.40		0.00
$O_{As}$	+1	1.50	0.09	1.31	0.07	0.19
	0	2.20		2.16		0.04
	-1	3.18	0.12	3.16	0.09	0.02
$(As_{Ga})-O_{As}$	+1	0.83	0.08	0.74	0.08	0.09
	-1	3.06	0.19	3.06	0.10	0.00
$(As_{Ga})_2-O_{As}$	+1	0.98	0.12	1.00	0.08	0.02
	-1	3.17	0.13	3.28	0.08	0.11

TABLE IV. Charge transition levels ( $\epsilon_{q/q'}$ ) for a series of relevant defects, including the most stable O defects and their dissociation products, as calculated at the PBE level of theory with 64-atom and 216-atom supercells and a  $2 \times 2 \times 2$   $\mathbf{k}$ -point mesh. The last column gives the difference  $\Delta \epsilon_{q/q'}$  between the charge transition levels obtained with the two supercell sizes. The defect levels are referred to the VBM obtained in a HSE calculation and aligned through the average electrostatic potential. Energies are in eV.

Defect	$\epsilon_{q/q'}$	64-atom	216-atom	$\Delta \epsilon_{q/q'}$
$V_{Ga}/V_{As}-As_{Ga}$	$\epsilon_{+3/-2}$	0.23	0.23	0.00
	$\epsilon_{-2/-3}$	0.99	0.87	0.12
$V_{As}-2As_{Ga}/V_{Ga}-As_{Ga}$	$\epsilon_{+1/-1}$	0.55	0.62	0.12
	$\epsilon_{-1/-2}$	1.18	1.22	0.04
$O_{As}$	$\epsilon_{+1/0}$	0.70	0.85	0.15
	$\epsilon_{0/-1}$	0.98	1.00	0.02
$(As_{Ga})-O_{As}$	$\epsilon_{+1/-1}$	1.12	1.16	0.04
$(As_{Ga})_2-O_{As}$	$\epsilon_{+1/-1}$	1.10	1.14	0.04

$\mathbf{k}$ -point mesh yield results sufficiently accurate for this study. We note that this conclusion apparently conflicts with the generally adopted setup which consists of using 216-atom supercells [62,85,86]. However, in the case of interstitial As and Ga defects in GaAs, it was already pointed by Schick *et al.* that converged results could be obtained with 64-atom supercells [87]. Moreover, we note that our results for the bistable  $V_{Ga}/V_{As}-As_{Ga}$  defect compare well with previous calculations by Schultz and von Lilienfeld [62]. In particular, the charge transition levels  $\epsilon_{+3/-2}$  and  $\epsilon_{-2/-3}$  found in Ref. [62] at 0.38 and 0.80 eV, respectively, do not deviate more than 0.15 eV from our results reported in Table IV. In Ref. [85], the bistability is not considered, but the  $\epsilon_{-2/-3}$  of  $V_{Ga}$  is found at 0.55 eV from the PBE VBM, in good agreement with the value of 0.58 eV that we obtained for the same alignment.

We finally perform convergence checks at the hybrid functional level for one representative defect, the  $(As_{Ga})_2-O_{As}$  defect. We here examine whether the computational setup identified within PBE also leads to converged results with HSE. First, we investigate the effect of  $\mathbf{k}$ -point density. For a 64-atom supercell, we increase the  $\mathbf{k}$ -point mesh from  $2 \times 2 \times 2$  (first column in Table V) to  $3 \times 3 \times 3$  (second column). The formation energies of the +1 and -1 charge states are found to undergo negligible shifts of 7 and 23 meV, respectively. This ensures that the density of the  $2 \times 2 \times 2$   $\mathbf{k}$ -point mesh is adequate to yield formation energies and charge transition levels with HSE sufficiently converged for this study (cf. Table V). Second, we consider the effect of neglecting structural relaxation at the HSE level. For reference, we obtain a configuration of the  $(As_{Ga})_2-O_{As}$  defect corresponding to the HSE structure in a 216-atom supercell, following the scheme described in the benchmark study of Ref. [43]. The formation energies obtained in this way (third column in Table V) differ by at most 85 meV from those calculated with the computational setup adopted in this work (first column), namely, with structural relaxations achieved with PBE in a 64-atom supercell. This agreement confirms that 64-atom supercells and relaxations within PBE are sufficient to yield converged electronic properties of the defect within

TABLE V. Charge transition levels ( $\epsilon_{q/q'}$ ) and formation energies ( $E_f$ ) calculated at the HSE level of theory with different cell sizes and  $\mathbf{k}$ -point meshes, for the most stable O defect identified in this work ( $\text{As}_{\text{Ga}})_2\text{-O}_{\text{As}}$ . The calculations are performed for defect geometries obtained at the PBE level with 64-atom cells and at the HSE level with 216-atom cells. Two  $\mathbf{k}$ -point meshes are used. The  $2 \times 2 \times 2$   $\mathbf{k}$ -point mesh for the 216-atom supercell shows the same density as the  $3 \times 3 \times 3$   $\mathbf{k}$ -point mesh for the 64-atom supercell. For comparison, we also show corresponding energies for the As antisite from Refs. [43,83]. Energies are given in eV.

	PBE 64-atom		HSE 216-atom
	$2 \times 2 \times 2$	$3 \times 3 \times 3$	$2 \times 2 \times 2$
$(\text{As}_{\text{Ga}})_2\text{-O}_{\text{As}}$			
$\epsilon_{+1/-1}$	1.17	1.17	1.21
$E_f(q = +1)$	1.50	1.51	1.41
$E_f(q = -1)$	3.84	3.84	3.84
$\text{As}_{\text{Ga}}$			
$\epsilon_{+2/+1}$	0.46		0.51
$\epsilon_{+1/0}$	0.94		0.92
$E_f(q = +2)$	-0.10		0.09
$E_f(q = +1)$	0.36		0.60
$E_f(q = 0)$	1.30		1.52

HSE. The good agreement between the results based on HSE and PBE relaxed structures stems from the localized nature of the defect state, which is equivalently described at these levels of theory provided the defect level falls in the band gap [43]. For comparison, we also report in Table V the results of similar convergence tests performed for the  $\text{As}_{\text{Ga}}$  antisite defect in Refs. [43,83]. These results further confirm the present analysis showing errors of similar size.

In summary, on the basis of the present convergence checks, we estimate that our scheme carries an accuracy of 0.3 eV for defect formation energies, the principal source of error arising from the treatment of the Ga  $3d$  electrons. For defect charge transition levels, our tests show a maximal error of 0.15 eV, resulting from long-range structural effects extending beyond the 64-atom supercell. The present accuracy assessment for O defects in GaAs yields overall similar conclusions as the one performed in Ref. [43] for the  $\text{As}_{\text{Ga}}$  antisite defect.

### III. OXYGEN DEFECTS

#### A. $\text{O}_b$

In the bridging interstitial defect  $\text{O}_b$ , the O atom binds to an As atom and a Ga atom of the regular GaAs network, as shown in Fig. 3(a). In the relaxed structure, the As-O and Ga-O bond lengths are 1.81 and 1.83 Å, respectively, while the As-O-Ga bond angle takes the value of  $129^\circ$ , in good agreement with previous theoretical studies [37,38]. In this stable defect configuration, one As atom in the second-neighbor shell of the O atom belongs to the plane defined by the As-O-Ga unit. During a complete rotation around the axis of the original Ga-As bond, three equivalent defect configurations are found. Through nudged elastic band calculations with 12 images and one climbing image [88], we find that the energy barrier between two equivalent minima amounts to  $\sim 15$  meV. The

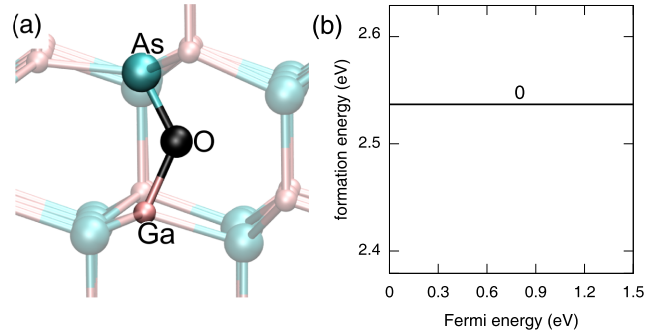


FIG. 3.  $\text{O}_b$  defect, in which the O atom occupies a bridging interstitial site: (a) relaxed structure and (b) formation energy vs Fermi energy.

transition state occurs when the As-O-Ga plane contains a second-neighbor Ga atom.

The  $\text{O}_b$  defect configuration is only stable in its neutral charge state, in agreement with experimental evidence [29] and a previous calculation [37]. The formation energy calculated with HSE is 2.54 eV, as shown in Fig. 3(b), and corresponds to the lowest value among the interstitial defects considered in this work.

For completeness, we also investigate the bridging configuration proposed by Taguchi and Kageshima [39] and indeed find an equilibrium configuration. However, the identified structure does not correspond to a local minimum and readily relaxes towards that of the  $\text{O}_b$  defect upon a small displacement of the O atom. We remark that the equilibrium configuration proposed by Taguchi and Kageshima corresponds to the symmetrical transition state for diffusion jumps between nearby  $\text{O}_b$  configurations, similarly to the Y configuration for O diffusion in silicon [89,90].

#### B. $\text{O}_i\text{-Ga}_4$ and $\text{O}_i\text{-As}_4$

The zinc-blende structure of GaAs presents two tetrahedral interstitial sites in which interstitial oxygen ( $\text{O}_i$ ) can be incorporated, one enclosed by four As atoms ( $\text{O}_i\text{-As}_4$ ) and one by four Ga atoms ( $\text{O}_i\text{-Ga}_4$ ). By carrying out structural relaxations of the  $\text{O}_i\text{-As}_4$  defect in a 216-atom supercell, we find that the  $\text{O}_i\text{-As}_4$  defect is unstable and relaxes without any barriers to  $\text{O}_i\text{-Ga}_4$  defect structure. This spontaneous transition is not observed in the 64-atom supercell, as this cell is too small to describe the important deformations undergone by the GaAs network upon the hopping of the O atom from one interstitial site to the other. We note that the higher stability of the  $\text{O}_i\text{-Ga}_4$  site can be rationalized through electrostatic arguments.

In the  $\text{O}_i\text{-Ga}_4$  defect, the O atom is located at the tetrahedral site and forms four equivalent O-Ga bonds with bond lengths of 2.05 Å and four Ga-O-Ga angles of  $109^\circ$ , as shown in Fig. 4(a). This structure agrees well with previous semilocal calculations [38]. Our hybrid functional calculations indicate that only the neutral charge state is stable. In particular, the negatively charged states (from  $-1$  to  $-3$ ) do not give rise to localized charge states, as can be inferred from the behavior of the electrostatic potential calculated upon the addition of electrons [cf. Fig. 1(b) for the  $-1$  charge state]. This assessment is at variance with previous studies, in which the charge localization

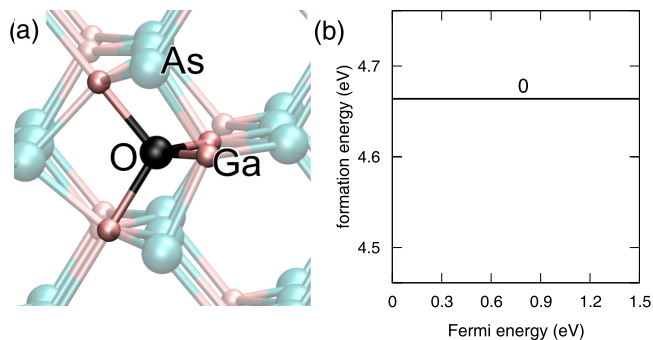


FIG. 4. Interstitial  $O_i$ - $Ga_4$  defect: (a) relaxed structure and (b) formation energy vs Fermi energy.

was not considered as a criterion for defining the stability of a given charge state [38]. The defect formation energy calculated with the HSE hybrid functional is 4.66 eV, as shown in Fig. 4(b). By comparing the formation energy of the present defect with that of the  $O_b$  defect, we find a difference of more than  $\sim 2$  eV, which clearly disfavors the incorporation of oxygen in the tetrahedral  $O_i$ - $Ga_4$  configuration.

### C. $O_{As}$

The  $O_{As}$  defect was initially assumed as origin of the experimentally identified Ga-O-Ga structure, mostly because of the analogy with the VO center in silicon [27]. This assignment was supported by semilocal density functional calculations [36]. The O was found to occupy an off-center position and to bind two Ga atoms [36]. Moreover, the charge state  $-2$  was found to be metastable in agreement with the observation of metastability associated with the  $B'$  band in the LVM spectra [36]. These results were confirmed in later studies, which located the  $-1/-3$  charge transition level at  $\sim 0.5$  eV below the CBM under the assumption that the calculated valence band edge could be aligned to the experimental one [37,38]. Recently, through the use of hybrid functionals, we showed that the structural and electronic properties of the  $O_{As}$  defect cannot account for the experimentally identified Ga-O-Ga defect [46]. Here, we briefly summarize the main properties of the  $O_{As}$  defect and refer to Ref. [46] for a more detailed description.

In the charge state  $+1$ , the O atom occupies the center of the As vacancy and forms four equivalent O-Ga bonds with bond lengths of 2.17 Å. This structure is also stable in the neutral charge defect state, which presents an unpaired electron. In the charge state  $-1$ , the O atom relaxes into a structure of lower symmetry ( $C_{2v}$ ), as shown in Fig. 5(a). The O atom then binds two Ga atoms with bond lengths of 1.87 Å, while the other two Ga atoms of the defective site form a Ga-Ga bond with a length of 2.87 Å. We note that the stable defect structures satisfy the electron counting rule [46]. According to this rule, the available electrons can be accounted for by considering that fourfold-coordinated Ga and As atoms contribute to each bond in which they are involved with  $\frac{3}{4}$  and  $\frac{5}{4}$  electrons, respectively [91].

The formation energies of the charge states  $+1$ ,  $0$ , and  $-1$  of the  $O_{As}$  defect are shown in Fig. 5(b). The results correspond to those that we previously reported in Ref. [46], except for the use of a different reference for the O chemical potential.

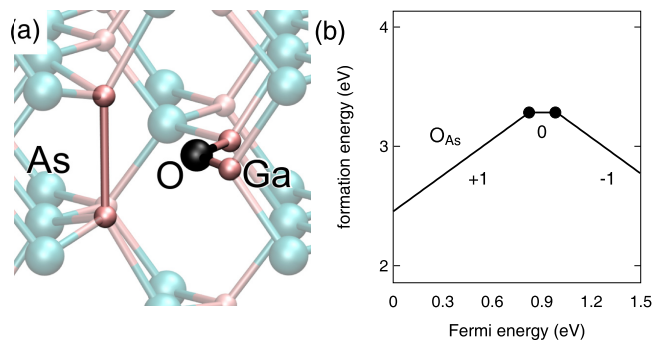


FIG. 5.  $O_{As}$  defect: (a) relaxed structure in the charge state  $-1$ , and (b) formation energies vs Fermi energy.

The finite-size corrections applied to the formation energies of charge states  $+1$  and  $-1$  amount to 0.12 and 0.15 eV, respectively. The calculated  $+1/0$  and  $0/-1$  charge transition levels lie at 0.82 and 0.99 eV above the VBM, respectively. The stability of both positive and negative charge states indicates that the defect is amphoteric supporting Fermi-level pinning at  $\sim 0.9$  eV above VBM [9], in satisfactory agreement with the experimental pinning level at  $\sim 1.1$  eV above the VBM [13]. However, the present defect neither shows negative- $U$  behavior nor a stable Ga-O-Ga structural unit in all three charge states, as observed in experiment [31]. Therefore, the  $O_{As}$  defect cannot account for the experimental characterization of the Ga-O-Ga defect.

For reference, we report in Table VI the defect formation energies for Fermi energies at the VBM ( $p$ -type) and at the CBM ( $n$ -type), calculated in both As- and Ga-rich conditions. When Ga-rich conditions are assumed,  $\mu_{Ga}$  is taken from bulk Ga in the solid orthorhombic phase, whereas  $\mu_{As}$  and  $\mu_O$  result from the equilibrium conditions of GaAs and  $\beta$ - $Ga_2O_3$ , respectively. When changing the atomic chemical potentials taken as reference, the defect formation energies undergo a rigid shift without affecting the positions of the charge transition levels.

### D. $O_{Ga}$

In the  $O_{Ga}$  defect, the O atom is centrally located in the Ga vacancy, where it forms four equivalent O-As bonds with lengths of 2.26 Å and four As-O-As angles of  $109^\circ$ . This

TABLE VI. Formation energies of the substitutional  $O_{As}$  and  $O_{Ga}$  defects in various charge states, as obtained with the HSE hybrid functional for  $p$ - and  $n$ -type GaAs, in both As- and Ga-rich conditions. Energies are in eV.

Charge	Condition	$O_{As}$		$O_{Ga}$	
		$p$ -type	$n$ -type	$p$ -type	$n$ -type
-1	Ga-rich	3.92	2.39	8.82	7.29
	As-rich	4.30	2.77	6.92	5.39
0	Ga-rich	2.93	2.93	7.82	7.82
	As-rich	3.31	3.31	5.92	5.92
+1	Ga-rich	2.11	3.64	7.40	8.93
	As-rich	2.49	4.02	5.50	7.03

atomic structure does not undergo significant variations upon charging.

Stable charge states are the singly positive, the neutral, and the singly negative charge states. The charged defect states carry an even number of electrons, whereas the neutral charge state shows an unpaired electron. In As-rich conditions, the formation energy of this defect varies between 5.39 and 5.92 eV, which make its formation unfavorable. Therefore, we refrain from graphically illustrating the calculated formation energies. Calculated defect formation energies for various conditions are summarized in Table VI. From the comparison between the formation energies of the two substitutional defects  $O_{As}$  and  $O_{Ga}$ , we infer that the former defect is energetically preferred.

### E. $(2 O)_{As}$

In order to saturate all the Ga dangling bonds (DBs) facing an As vacancy, it is natural to consider two O atoms leading to the  $(2 O)_{As}$  defect. The electron counting rule suggests that two twofold-coordinated O atoms could saturate the exposed Ga dangling bonds in the charge state  $-1$ . However, upon direct relaxation in this charge state, we obtain two threefold-coordinated O atoms, with one of the O atoms having moved to a nearby interstitial site.

In order to explore the configurational space available to the two O atoms, we carry out molecular dynamics simulations with PBE. We perform runs of 5 ps in both the neutral and  $-1$  charge states at three different temperatures (300, 500, and 800 K). The adopted thermostat rescales the velocities when the cumulative average temperature moves out of a predefined temperature window. In addition to the structure found by direct relaxation, the molecular dynamics simulations identify a second structure, in which the O atoms are also threefold coordinated with Ga.

In the second configuration, only the Ga atoms facing the vacancy participate to the bonding, giving two fourfold- and two fivefold-coordinated Ga atoms, as shown in Fig. 6(a). Each O atom forms one short bond with a fourfold-coordinated Ga atom (1.88 Å) and two long bonds with the two fivefold-coordinated Ga atoms (2.00 Å). Oxygen bond angles are  $125^\circ$  in Ga-O-Ga units involving one fourfold- and one fivefold-

coordinated Ga atom, and  $94^\circ$  in Ga-O-Ga units involving two fivefold-coordinated Ga atoms.

To rationalize the electronic behavior of these defect structures, we adopt an analysis based on maximally localized Wannier functions (WF), which allow for a real-space representation of the electron localization [92]. In both  $(2 O)_{As}$  defect structures, the O atoms are surrounded by four WF centers, three of which point towards a Ga atom and correspond to Ga-O bonds, as shown in Fig. 6(a). The fourth WF center lies closer to the O atom and corresponds to a lone pair. Application of the electron counting rule reveals that both  $(2 O)_{As}$  defect structures require one extra electron in order to doubly occupy all the bonds. Indeed, the Kohn-Sham energy of the Ga-O bonds are deep in the valence band and the only stable defect state is the charge state  $-1$  [cf. Fig. 6(b)].

For the determination of defect formation energies, we realize that the 64-atom supercell is too small to observe complete screening of the defect charge as expected for localized defect states [45]. To ensure proper screening behavior, we thus use 512-atom supercells with the sole  $\Gamma$  point. This  $\mathbf{k}$ -point sampling is equivalent to that used for the other oxygen-related defects, thereby allowing direct comparisons of formation energies. The configuration identified by molecular dynamics is the most stable one for the  $(2 O)_{As}$  defect. Its formation energy is displayed in Fig. 6(b). The applied finite-size correction is 0.09 eV. The structure achieved by direct relaxation lies 0.45 eV higher in energy. We note that, with respect to the  $O_{As}$  defect, the electrical properties undergo significant variation upon the capture of a second O atom. The amphoteric nature of the  $O_{As}$  defect disappears and the  $-1$  charge state is the only stable defect state.

### F. $As_{Ga}-O_{As}$

We consider the  $As_{Ga}-O_{As}$  defect complex which consists of an  $O_{As}$  defect bound to an  $As_{Ga}$  antisite defect in its first-neighbor shell. In the charge state  $+1$ , the O atom binds to three Ga atoms facing the arsenic vacancy  $V_{As}$  and forms three equivalent bonds with lengths of 1.98 Å [Fig. 7(a)]. The As atom in the antisite position forms three equivalent As-As bonds with lengths of 2.50 Å, leading to a global structure of  $C_{3v}$  symmetry. This As atom carries a lone pair, as confirmed through the calculation of maximally localized Wannier functions [Fig. 7(a)]. The electron counting rule is satisfied and all bonds are doubly occupied.

In the neutral charge state, the extra electron breaks the  $C_{3v}$  symmetry. Two of the O-Ga bonds shorten and one of the As-As bonds elongates, as shown in Fig. 7(b). Application of the electron counting rule implies a paramagnetic defect state with an unpaired electron, of which the charge density is illustrated in Fig. 7(b). This charge density shows antibonding character over the elongated As-As bond and bonding character between the antisite As atom and a nearby Ga atom.

In the charge state  $-1$ , the addition of a second electron drives the defect structure towards a closed-shell configuration which satisfies the electron counting rule [cf. Fig. 7(c)]. The analysis through WF centers reveals that the O atom is twofold coordinated (with two O-Ga bond lengths of 1.91 Å) and that the antisite As atom binds to two As atoms and one Ga atom.

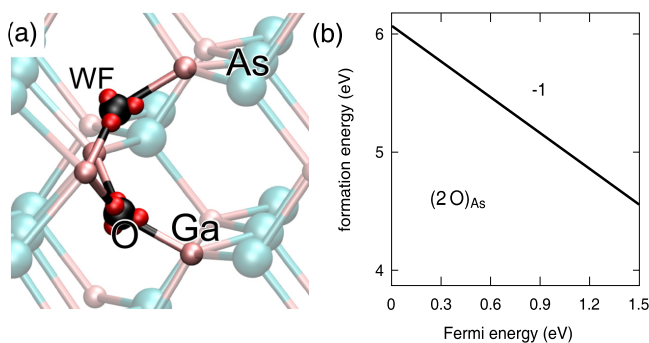


FIG. 6.  $(2 O)_{As}$  defect: (a) relaxed structure of the most stable configuration in the charge state  $-1$ , and (b) formation energies vs Fermi energy. In (a), the centers of relevant maximally localized Wannier functions are illustrated through small red spheres.

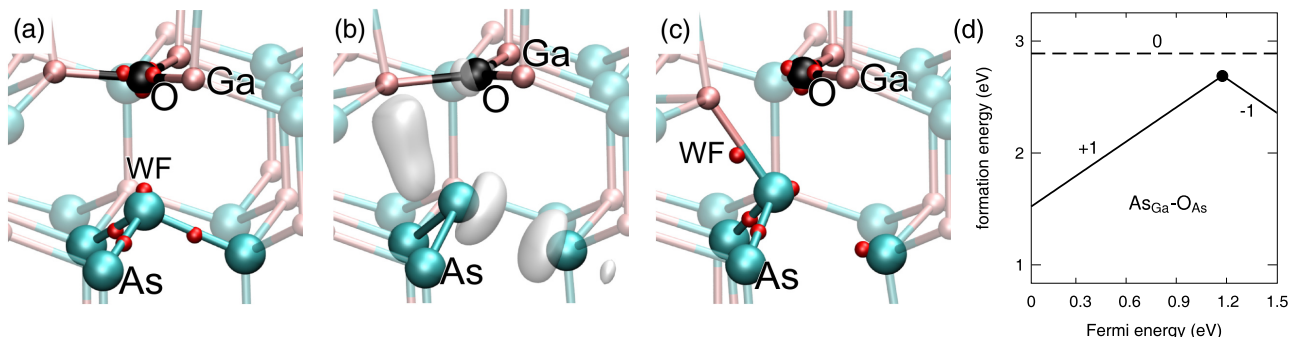
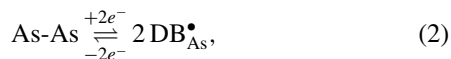


FIG. 7.  $AS_{Ga}-O_{As}$  defect: (a) relaxed structure in the charge state  $+1$ , (b) relaxed structure in the metastable neutral charge state with the density of the unpaired electron in transparency, (c) relaxed structure in the charge state  $-1$ , and (d) formation energies vs Fermi energy. The small red spheres in (a) and (c) indicate the center of the relevant maximally localized Wannier functions.

The breaking of the As-As bond leaves oppositely oriented lone pairs on the two As atoms [Fig. 7(c)].

The charge states  $+1$  and  $-1$  of the present defect are stable, while the neutral charge state is metastable, as can be seen from the defect formation energies reported in Fig. 7(d). Calculated finite-size corrections amount to 0.10 and 0.13 eV for charge states  $+1$  and  $-1$ , respectively. The  $AS_{Ga}-O_{As}$  defect shows amphoteric character and a charge transition level at 1.17 eV above the VBM, in good agreement with the energy at which the Fermi level is pinned experimentally [13,20]. The number and type of stable charge states, the paramagnetic character of the neutral charge state, and its metastable nature all agree with experimental observations for the Ga-O-Ga defect [29,31–33,35]. However, the Ga-O-Ga core structure only occurs in the charge state  $-1$  and transforms into a symmetrical O-Ga<sub>3</sub> structure in the charge state  $+1$ . This structural rearrangement disagrees with the experimental evidence that the Ga-O-Ga core persists in all three charge states [31,32]. We remark that the mechanism by which the  $AS_{Ga}-O_{As}$  defect complex captures and releases two electrons is analogous to that observed for the As-As dimer/DB defect [17,93]:



which has been invoked for explaining the Fermi-level pinning at GaAs surfaces and interfaces.

### G. $(AS_{Ga})_2-O_{As}$

The  $(AS_{Ga})_2-O_{As}$  defect structure was initially proposed by Pesola *et al.* [40] as origin of the experimentally identified Ga-O-Ga structure. To support this assignment, they showed that the defect is stable in its charge states  $+1$  and  $-1$ , while the neutral state is metastable, accounting for the observed negative- $U$  behavior of the defect. The Ga-O-Ga structural unit was found to be stable in all the charge states of the defect and the calculated vibrational frequencies to agree with the experimental characterization. More recently, a hybrid functional study yielded defect energies in agreement with experiment [47], further corroborating the assignment of the Ga-O-Ga structure to the  $(AS_{Ga})_2-O_{As}$  defect. In the following, we briefly summarize the main properties of the  $(AS_{Ga})_2-O_{As}$

defect. For a more detailed description, we refer the reader to Refs. [40,47].

In the charge state  $+1$ , each As atom occupying an antisite forms three As-As bonds and exposes a lone pair towards the O atom, resulting in a structure which satisfies the electron counting rule [47]. In the neutral charge state, two As-As bonds break and a bond is formed between the two As atoms located in the antisites. This structure holds an unpaired electron of which the charge density shows an antibonding character over the broken  $AS_{Ga}-As$  linkages and a bonding character between the two As atoms in the antisites [Fig. 8(a)]. In the charge state  $-1$ , the relaxed defect structure does not differ significantly from that of the neutral defect state, but the electron counting rule is again satisfied. The lone pairs carried by the two  $AS_{Ga}$  atoms turn away from the O atom, thereby reducing the steric effect on the O vibrational modes [47] and providing a simple explanation for the experimentally observed frequency difference between the defect charge states [31,32].

Figure 8(b) displays the formation energies of the various charge states of the  $(AS_{Ga})_2-O_{As}$  as a function of Fermi energy. The reported formation energies include finite-size corrections of 0.13 and 0.14 eV in the charge states  $+1$  and  $-1$ , respectively. From Fig. 8(b), it is seen that the defect is amphoteric providing a mechanism [9] by which the experimentally observed Fermi-level pinning [13,20,33] can be accounted for [47]. Indeed, the charge transition level calculated at

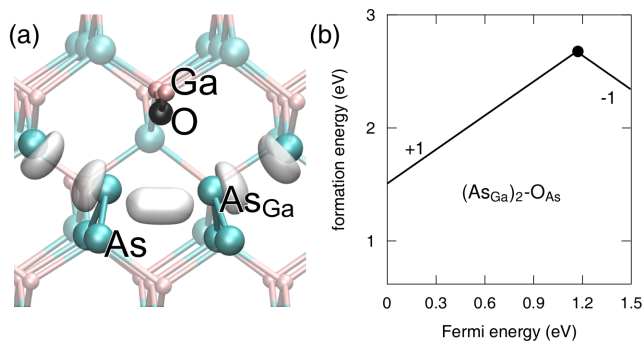


FIG. 8.  $(AS_{Ga})_2-O_{As}$  defect: (a) relaxed structure in the neutral charge state with the charge density of the unpaired electron in transparency, and (b) formation energies vs Fermi energy.

1.17 eV agrees well with the Fermi-level pinning measured at 1.10–1.17 eV (Refs. [13,33]). An analysis of the optical transitions between charge states [47] similarly confirms that the energetic description achieved for the  $(\text{As}_{\text{Ga}})_2\text{-O}_{\text{As}}$  defect accurately accounts for the experimental characterization [13]. We note that the atomic transformation underlying the amphoteric behavior of the  $(\text{As}_{\text{Ga}})_2\text{-O}_{\text{As}}$  defect corresponds to the bistability of the As-As dimer/DB defect [17]. Indeed, the structural rearrangements ensuing the capture/release of two electrons can be condensed to the reaction in Eq. (2) [17,93].

#### IV. DEFECT DISSOCIATION

Among the oxygen defects considered in this work, the  $\text{As}_{\text{Ga}}\text{-O}_{\text{As}}$  and the  $(\text{As}_{\text{Ga}})_2\text{-O}_{\text{As}}$  complexes show the lowest formation energies. In this section, we investigate the stability of these defect complexes against dissociation. Indeed, both these complexes could either dissociate an O atom or an  $\text{As}_{\text{Ga}}$  antisite. To address the dissociation process, we here focus on the dissociation of an O atom. The dissociation of an  $\text{As}_{\text{Ga}}$  antisite can be treated along the same lines.

We thus consider a defect complex  $DO$  corresponding to an unoxidized intrinsic defect  $D$  which has captured an O atom. The simplest examples are O substitutional defects which can be pictured as O atoms captured in vacancies. In order to assess whether a specific defect complex occurs, we here adopt two criteria [48].

The first criterion concerns the relative stability between the defect complex and its dissociation products. We define the complex dissociation energy ( $E_{\text{dissoc}}$ ) as a binding energy [48,94]

$$E_{\text{dissoc}} = -[E_f(DO) - E_f(D) - E_f(\text{O}_b)], \quad (3)$$

where the dissociation products are the isolated unoxidized defect  $D$  and the most stable interstitial O defect  $\text{O}_b$  corresponding to the bridging As-O-Ga configuration (Sec. III A). By this definition,  $E_{\text{dissoc}}$  is a function of Fermi energy. The sign of  $E_{\text{dissoc}}$  notifies whether the defect complex is stable upon dissociation. A positive value supports the stability of the defect complex, while a negative value indicates that the isolated dissociation products are favored and that the complex does not occur [48]. We note that  $E_{\text{dissoc}}$  does not depend on the references defining the chemical potentials. This stability criterion therefore holds irrespective of specific growth conditions.

The second criterion depends on the defect equilibrium concentration which is derived from the defect formation energy through the following relation [48]:

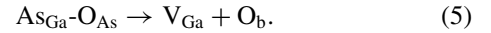
$$[X^q] = N_{\text{sites}} N_{\text{config}} \exp[-E_f(X^q)/kT], \quad (4)$$

where  $N_{\text{sites}}$  is the number of sites per unit volume in which the defect can be incorporated,  $N_{\text{config}}$  the number of equivalent defect configurations,  $k$  Boltzmann's constant, and  $T$  the temperature. The concentration of the  $DO$  complex dominates over that of the  $\text{O}_b$  defect when  $E_f(DO)$  is smaller than  $E_f(\text{O}_b)$ . This second criterion therefore informs us about the relevance of the defect complex concentration at thermal equilibrium. We note that, unlike the criterion based on the dissociation energy, the present one depends on the chemical potentials adopted in the definition of the defect formation energy [48]. Indeed, this

reflects the fact that the ratio between the concentrations of different defects depends on growth conditions.

#### A. Oxygen dissociation

The stability of the  $\text{As}_{\text{Ga}}\text{-O}_{\text{As}}$  defect complex can be examined by comparing its formation energy with those of its dissociation products, the isolated gallium vacancy  $V_{\text{Ga}}$  and the isolated  $\text{O}_b$ , according to the reaction



In this decomposition, it should be accounted for that one of the dissociation products, the Ga vacancy, occurs in different structures depending on Fermi energy. Indeed, when the Fermi energy lies close to the VBM, the  $V_{\text{Ga}}$  defect relaxes to the  $V_{\text{As}}\text{-As}_{\text{Ga}}$  defect complex through the displacement of one of the As atoms facing the vacancy into the vacancy site [95]. We here calculate the formation energy of the bistable  $V_{\text{Ga}}/V_{\text{As}}\text{-As}_{\text{Ga}}$  defect at the same level of theory as the other O defects. Our description of this defect agrees with previous calculations at the semilocal level (cf. Sec. II C) [62]. The dissociation energy of the  $\text{As}_{\text{Ga}}\text{-O}_{\text{As}}$  complex shows positive values exceeding 3 eV in  $p$ -type condition [cf. Fig. 9(a)]. However, the dissociation energy decreases with Fermi energy, reaching negative values in  $n$ -type condition. Hence, the stability criterion for the  $\text{As}_{\text{Ga}}\text{-O}_{\text{As}}$  complex is fulfilled over almost the entire band gap, with the sole exception of a small energy region in the vicinity of the conduction band.

Under O doping conditions, the formation energy of the  $\text{As}_{\text{Ga}}\text{-O}_{\text{As}}$  defect should be lower than that of the  $\text{O}_b$  defect [Fig. 9(a)] to fulfill the second criterion for defect occurrence. This is indeed the case for all Fermi energies in the band gap, except for a small range around the defect charge transition level at 1.17 eV above the VBM, where the small differences between the formation energies of the  $\text{As}_{\text{Ga}}\text{-O}_{\text{As}}$  and  $\text{O}_b$  defects suggest that these two defects coexist.

For examining the stability of the  $(\text{As}_{\text{Ga}})_2\text{-O}_{\text{As}}$  defect, we consider the dissociation into the  $V_{\text{Ga}}\text{-As}_{\text{Ga}}$  defect complex and the  $\text{O}_b$  defect, according to

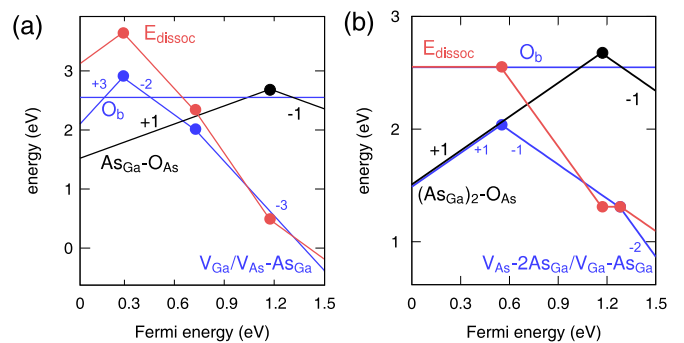


FIG. 9. Formation energy vs Fermi energy for two O defect complexes (black lines), (a)  $\text{As}_{\text{Ga}}\text{-O}_{\text{As}}$  and (b)  $(\text{As}_{\text{Ga}})_2\text{-O}_{\text{As}}$ , and their dissociation products (light blue). The dissociation products are defined by Eqs. (5) and (6). Corresponding binding energies are shown through red lines.

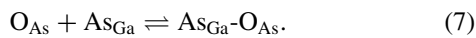
The  $V_{\text{Ga}}\text{-As}_{\text{Ga}}$  defect complex has already been studied in the literature for its possible role in the Fermi-level pinning of radiation-damaged GaAs [96]. It can be pictured as a  $\text{As}_{\text{Ga}}$  defect bonded to a  $V_{\text{Ga}}$  defect, which transforms into the  $V_{\text{As}}\text{-}2\text{As}_{\text{Ga}}$  structure upon the displacement of one As atom facing the Ga vacancy into the vacancy site [96]. The defect complex is found to be stable in the structure  $V_{\text{As}}\text{-}2\text{As}_{\text{Ga}}$  for the charge state  $+1$ , and in the structure  $V_{\text{Ga}}\text{-As}_{\text{Ga}}$  for the charge states  $-1$  and  $-2$  [cf. Fig. 9(b)].

The dissociation energy of the  $(\text{As}_{\text{Ga}})_2\text{-O}_{\text{As}}$  defect is displayed in Fig. 9(b). It is found to be larger than 1 eV for all Fermi energies within the band gap, guaranteeing defect stability against dissociation. As far as the second criterion for defect occurrence is concerned, we note that the formation energy of the  $(\text{As}_{\text{Ga}})_2\text{-O}_{\text{As}}$  defect is smaller than that of the  $\text{O}_{\text{b}}$  defect for all Fermi energies in the band gap, but a small energy region around the defect charge transition level at 1.17 eV above the VBM. Under oxygen doping conditions, the  $(\text{As}_{\text{Ga}})_2\text{-O}_{\text{As}}$  defect complex is thus expected to be relevant. As its amphoteric nature leads to Fermi-level pinning at the  $+1/-1$  charge transition level [9], one should expect that the  $(\text{As}_{\text{Ga}})_2\text{-O}_{\text{As}}$  and  $\text{O}_{\text{b}}$  defects coexist due their close formation energies at these Fermi energies. This assessment is consistent with experimental observations inferring that the  $\text{O}_{\text{b}}$  and the Ga-O-Ga defects occur simultaneously [27,29].

The present analysis leads to the conclusion that the  $\text{As}_{\text{Ga}}\text{-O}_{\text{As}}$  and  $(\text{As}_{\text{Ga}})_2\text{-O}_{\text{As}}$  defect complexes show very similar behavior with respect to O dissociation. Both complexes are stable against O dissociation and are expected to coexist with  $\text{O}_{\text{b}}$  defects.

### B. $\text{As}_{\text{Ga}}$ dissociation

The  $\text{As}_{\text{Ga}}\text{-O}_{\text{As}}$  and  $(\text{As}_{\text{Ga}})_2\text{-O}_{\text{As}}$  defect complexes could also dissociate As antisite defects. Indeed, the  $\text{As}_{\text{Ga}}\text{-O}_{\text{As}}$  defect complex can be pictured as an  $\text{O}_{\text{As}}$  defect, to which a first  $\text{As}_{\text{Ga}}$  defect attaches,



The  $(\text{As}_{\text{Ga}})_2\text{-O}_{\text{As}}$  complex then results from the attachment of a second As antisite,



At thermal equilibrium, the concentrations of the  $\text{As}_{\text{Ga}}\text{-O}_{\text{As}}$  and  $(\text{As}_{\text{Ga}})_2\text{-O}_{\text{As}}$  complexes are comparable to each other due to their very close formation energies (cf. Fig. 10). However, their relative concentration would be different when we consider cooled-down conditions following a growth process at higher temperature [48]. To evaluate the binding energy for the attachment of an antisite, we compare in Fig. 10 the formation energies of  $(\text{As}_{\text{Ga}})_2\text{-O}_{\text{As}}$  with those of its dissociation products  $\text{As}_{\text{Ga}}\text{-O}_{\text{As}}$  and the isolated  $\text{As}_{\text{Ga}}$ . The binding energy  $E_{\text{b}}$ , calculated in the same way as the dissociation energy given in Eq. (3), is essentially positive over the whole range of Fermi energies in the band gap, indicating stability of the  $(\text{As}_{\text{Ga}})_2\text{-O}_{\text{As}}$  complex. More importantly, this assessment holds in correspondence of the charge transition levels of the defects at about 1.1 eV above the VBM, where the Fermi energy is expected to be pinned. At this value of

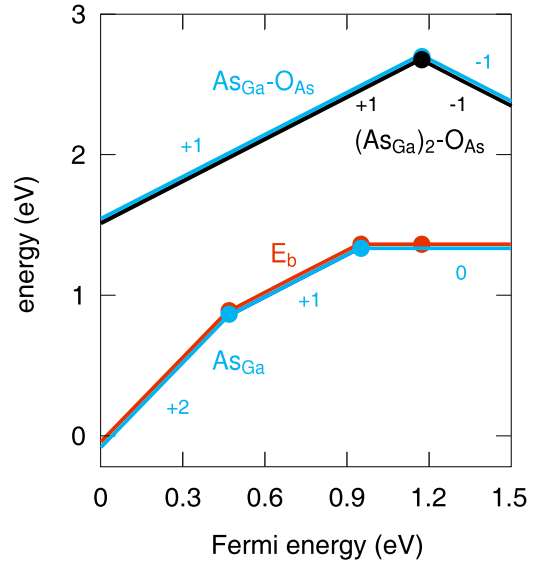


FIG. 10. Formation energy vs Fermi energy for the  $(\text{As}_{\text{Ga}})_2\text{-O}_{\text{As}}$  defect complex (black) and for its dissociation products  $\text{As}_{\text{Ga}}\text{-O}_{\text{As}}$  and  $\text{As}_{\text{Ga}}$  (light blue) according to reaction (8). The corresponding binding energy  $E_{\text{b}}$  is also shown (red). The formation energies of  $(\text{As}_{\text{Ga}})_2\text{-O}_{\text{As}}$  and  $\text{As}_{\text{Ga}}\text{-O}_{\text{As}}$  are very close. Consequently,  $E_{\text{b}}$  essentially coincides with the formation energy of  $\text{As}_{\text{Ga}}$ .

the Fermi energy,  $(\text{As}_{\text{Ga}})_2\text{-O}_{\text{As}}$  is 1.35 eV more stable than  $\text{As}_{\text{Ga}}\text{-O}_{\text{As}}$  with an isolated  $\text{As}_{\text{Ga}}$ .

To determine the effect of these binding energies on the relative concentrations of these two complexes, we proceed as follows. Following Eq. (4), we express the thermodynamic equilibrium concentration of isolated As antisites  $[\text{As}_{\text{Ga}}]$  at the growth temperature  $T_{\text{g}}$ :

$$[\text{As}_{\text{Ga}}] = N_{\text{sites}} \exp[-E_{\text{f}}(\text{As}_{\text{Ga}})/kT_{\text{g}}]. \quad (9)$$

Due to its small formation energy, the  $\text{As}_{\text{Ga}}$  is the dominant defect [72]. We assume that this concentration remains unmodified upon cooling down to lower temperatures and that it is essentially unaffected by reactions (7) and (8). In this picture, we assume that the available  $\text{As}_{\text{Ga}}$  can diffuse in the GaAs lattice as an isolated species or be bound within the  $\text{As}_{\text{Ga}}\text{-O}_{\text{As}}$  and  $(\text{As}_{\text{Ga}})_2\text{-O}_{\text{As}}$  complexes. Additionally, we have that

$$[\text{As}_{\text{Ga}}\text{-O}_{\text{As}}] + [(\text{As}_{\text{Ga}})_2\text{-O}_{\text{As}}] = C, \quad (10)$$

where the concentration  $C$  is determined at the growth temperature and remains fixed when the temperature decreases. Focusing on reaction (8), the mass action law at the cooled-down temperature  $T$  reads as

$$\frac{[(\text{As}_{\text{Ga}})_2\text{-O}_{\text{As}}]}{[\text{As}_{\text{Ga}}\text{-O}_{\text{As}}] \cdot [\text{As}_{\text{Ga}}]} = \frac{N_{\text{config}2}}{N_{\text{sites}}N_{\text{config}1}} \exp(E_{\text{b}}/kT), \quad (11)$$

where  $N_{\text{config}1}$  and  $N_{\text{config}2}$  are numbers of the same order, corresponding to the number of equivalent defect configurations for  $\text{As}_{\text{Ga}}\text{-O}_{\text{As}}$  and  $(\text{As}_{\text{Ga}})_2\text{-O}_{\text{As}}$ , respectively.

Using Eqs. (11) and (10), we obtain

$$[(\text{As}_{\text{Ga}})_2\text{-O}_{\text{As}}] = \frac{\alpha}{1 + \alpha} C, \quad (12)$$

with

$$\alpha = [\text{As}_{\text{Ga}}] \frac{N_{\text{config}2}}{N_{\text{sites}} N_{\text{config}1}} \exp(E_b/kT). \quad (13)$$

Since  $N_{\text{config}1} \approx N_{\text{config}2}$ , this expression simplifies to

$$\alpha \approx \exp[-E_f(\text{As}_{\text{Ga}})/kT_g + E_b/kT]. \quad (14)$$

Two extreme conditions can be identified. When  $\alpha \gg 1$ ,  $[(\text{As}_{\text{Ga}})_2\text{-O}_{\text{As}}] = C$  implying that all oxygen defects are in the form  $(\text{As}_{\text{Ga}})_2\text{-O}_{\text{As}}$ . At variance, for  $\alpha \ll 1$ ,  $[(\text{As}_{\text{Ga}})_2\text{-O}_{\text{As}}] \ll C$  and all oxygen atoms are in the form  $\text{As}_{\text{Ga}}\text{-O}_{\text{As}}$ .

In the case of interest to this work, we infer from Fig. 10 that  $E_f(\text{As}_{\text{Ga}}) \cong E_b$  leading to the preferential formation of  $(\text{As}_{\text{Ga}})_2\text{-O}_{\text{As}}$  for  $T < T_g$ . This result disfavors the formation of the  $\text{As}_{\text{Ga}}\text{-O}_{\text{As}}$  complex, which can thus be dismissed from the analysis.

## V. CONCLUSIONS

Using a state-of-the-art hybrid functional scheme, we calculated formation energies and charge transition levels of several O defects in GaAs. The calculated formation energies are summarized in Fig. 11. The most stable oxygen defects are the  $\text{O}_b$  defect and the O substitutional to As attached to either one ( $\text{As}_{\text{Ga}}\text{-O}_{\text{As}}$ ) or two  $[(\text{As}_{\text{Ga}})_2\text{-O}_{\text{As}}]$  As antisites. The  $\text{O}_b$  defect is electrically inactive with a formation energy of 2.54 eV. The  $\text{As}_{\text{Ga}}\text{-O}_{\text{As}}$  and  $(\text{As}_{\text{Ga}})_2\text{-O}_{\text{As}}$  defects show essentially equivalent energetics. They are both stable in the charge states +1 and -1, and both have formation energies of 1.55 and 2.33 eV in  $p$ - and  $n$ -type conditions,

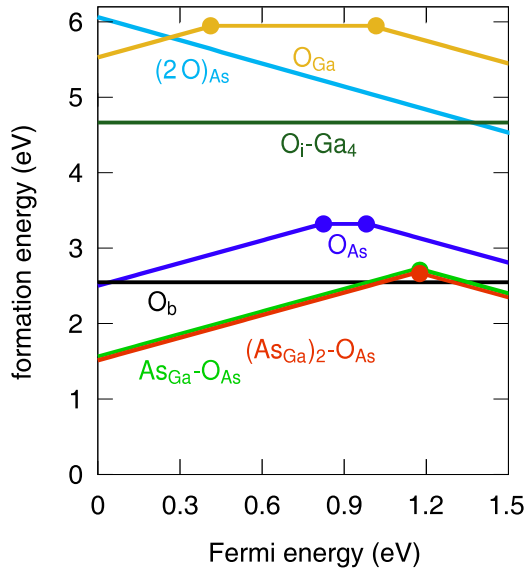


FIG. 11. Formation energy vs Fermi energy for the bridging interstitial oxygen defect  $\text{O}_b$  (black), the  $\text{O}_i\text{-Ga}_4$  defect (dark green), the  $\text{O}_{\text{Ga}}$  defect (yellow), the  $\text{O}_{\text{As}}$  defect (dark blue), the  $(2\text{O})_{\text{As}}$  defect (light blue), the  $\text{As}_{\text{Ga}}\text{-O}_{\text{As}}$  defect complex (light green), and the  $(\text{As}_{\text{Ga}})_2\text{-O}_{\text{As}}$  defect complex (red). As-rich conditions are assumed.

respectively. Their charge transition level at 1.17 eV above VBM is in good agreement with the experimental pinning level [13].

For these most stable oxygen defects, we investigated their stability against O dissociation as well as the relevance of their concentration at thermodynamic equilibrium. The defect stability was determined from the difference between the defect formation energy and those of its dissociation products. For the relevance of the defect concentration at thermodynamic equilibrium, we adopted a criterion which consists in comparing the defect formation energy with that of the most stable O interstitial defect, i.e., the  $\text{O}_b$  defect. Both defects were found to be stable against oxygen dissociation and at the thermodynamic equilibrium they are expected to coexist with the  $\text{O}_b$  defect for Fermi energies close to the pinning level. We then similarly considered the dissociation of As antisites, finding that the  $(\text{As}_{\text{Ga}})_2\text{-O}_{\text{As}}$  complex is expected to dominate upon cooling down.

The formation energies of the other defects considered in this work are larger than that of the  $\text{O}_b$  defect, indicating that their formation is unfavorable. In particular, the formation energy of the isolated  $\text{O}_{\text{As}}$  defect is higher by  $\sim 0.5$  eV than that of defect complexes in which the  $\text{O}_{\text{As}}$  defect is attached to one or two As antisites. The acceptor  $(2\text{O})_{\text{As}}$  defect, in which two O atoms are captured within the cavity of an As vacancy, is stable in the charge state  $-1$  across the full band gap, with formation energies ranging between  $\sim 4.5$  and  $\sim 6$  eV. The interstitial  $\text{O-Ga}_4$  defect is neutral and its formation involves a cost of 4.7 eV, more than 2 eV larger than that of the  $\text{O}_b$  defect, while the  $\text{O-As}_4$  defect has been found to be unstable and to spontaneously transform into the  $\text{O-Ga}_4$  defect. Finally, the substitutional  $\text{O}_{\text{Ga}}$  defect shows a formation energy ranging between 5.5 and 6 eV, about 3 eV larger than that of the other substitutional defect  $\text{O}_{\text{As}}$ , in both  $p$ - and  $n$ -type conditions. Our calculations generally show that the defects with the lowest formation energies are characterized by O-Ga bonds, in agreement with the higher stability of Ga oxides with respect to As oxides [97,98].

In conclusion, we have shown that the  $(\text{As}_{\text{Ga}})_2\text{-O}_{\text{As}}$  defect complex corresponds to the dominant oxygen defect in GaAs. The only competing O defect is the bridging oxygen interstitial ( $\text{O}_b$ ), which shows close formation energies in correspondence of the charge transition level of the  $(\text{As}_{\text{Ga}})_2\text{-O}_{\text{As}}$  complex. Since the Fermi level is found to pin in correspondence of this defect level, this finding suggests that the  $(\text{As}_{\text{Ga}})_2\text{-O}_{\text{As}}$  and  $\text{O}_b$  could coexist, in accord with experimental observations [27,29]. Furthermore, our work also shows that this defect complex is stable against both the dissociation of oxygen and the detachment of  $\text{As}_{\text{Ga}}$  antisites. These results corroborate the assignment of the Ga-O-Ga defect identified experimentally to the  $(\text{As}_{\text{Ga}})_2\text{-O}_{\text{As}}$  complex.

## ACKNOWLEDGMENTS

The authors thank H.-P. Komsa for making unpublished results [83] available concerning the benchmark study of the  $\text{As}_{\text{Ga}}$  defect [43]. Financial support is acknowledged from the Swiss National Science Foundation (Grant No. 200020-152799). We used computational resources of CSCS and CSEA-EPFL.

- [1] A. Krishnamoorthy and D. Miller, *IEEE J. Sel. Top. Quantum Electron.* **2**, 55 (1996).
- [2] J. A. del Alamo, *Nature (London)* **479**, 317 (2011).
- [3] J. Nah, H. Fang, C. Wang, K. Takei, M. H. Lee, E. Plis, S. Krishna, and A. Javey, *Nano Lett.* **12**, 3592 (2012).
- [4] G. Brammertz, H. C. Lin, K. Martens, A.-R. Alian, C. Merckling, J. Penaud, D. Kohen, W.-E. Wang, S. Sioncke, A. Delabie, M. Meuris, M. R. Caymax, and M. Heyns, *ECS Trans.* **19**, 375 (2009).
- [5] G. Brammertz, H.-C. Lin, K. Martens, D. Mercier, S. Sioncke, A. Delabie, W. E. Wang, M. Caymax, M. Meuris, and M. Heyns, *Appl. Phys. Lett.* **93**, 183504 (2008).
- [6] W. E. Spicer, *J. Vac. Sci. Technol.* **16**, 1422 (1979).
- [7] W. Spicer, P. Chye, C. Garner, I. Lindau, and P. Pianetta, *Surf. Sci.* **86**, 763 (1979).
- [8] W. E. Spicer, I. Lindau, P. Skeath, C. Y. Su, and P. Chye, *Phys. Rev. Lett.* **44**, 420 (1980).
- [9] W. Walukiewicz, *J. Vac. Sci. Technol. B* **5**, 1062 (1987).
- [10] W. E. Spicer, Z. Liliental-Weber, E. Weber, N. Newman, T. Kendelewicz, R. Cao, C. McCants, P. Mahowald, K. Miyano, and I. Lindau, *J. Vac. Sci. Technol. B* **6**, 1245 (1988).
- [11] W. Walukiewicz, *Phys. Rev. B* **37**, 4760 (1988).
- [12] W. Walukiewicz, *Appl. Phys. Lett.* **54**, 2094 (1989).
- [13] H. C. Alt, *Phys. Rev. Lett.* **65**, 3421 (1990).
- [14] M. Hong, J. Kwo, A. R. Kortan, J. P. Mannaerts, and A. M. Sergent, *Science* **283**, 1897 (1999).
- [15] W. Walukiewicz, *Phys. B (Amsterdam)* **302-303**, 123 (2001).
- [16] Y. C. Chang, W. H. Chang, C. Merckling, J. Kwo, and M. Hong, *Appl. Phys. Lett.* **102**, 093506 (2013).
- [17] D. Colleoni, G. Miceli, and A. Pasquarello, *J. Phys.: Condens. Matter* **26**, 492202 (2014).
- [18] D. Colleoni and A. Pasquarello, *Appl. Phys. Lett.* **107**, 031605 (2015).
- [19] D. Colleoni, G. Miceli, and A. Pasquarello, *Microelectron. Eng.* **147**, 260 (2015).
- [20] M. Jordan, M. Linde, T. Hangleiter, and J. Spaeth, *Semicond. Sci. Technol* **7**, 731 (1992).
- [21] M. Luysberg, H. Sohn, A. Prasad, P. Specht, Z. Liliental-Weber, E. R. Weber, J. Gebauer, and R. Krause-Rehberg, *J. Appl. Phys.* **83**, 561 (1998).
- [22] C. Song, W. Ge, D. Jiang, and C. Hsu, *Appl. Phys. Lett.* **50**, 1666 (1987).
- [23] C. Song, B. Pajot, and F. Gendron, *J. Appl. Phys.* **67**, 7307 (1990).
- [24] M. Skowronski and R. E. Kremer, *J. Appl. Phys.* **69**, 7825 (1991).
- [25] M. Skowronski, *Phys. Rev. B* **46**, 9476 (1992).
- [26] M. Skowronski, *Mater. Sci. Forum* **83-87**, 377 (1992).
- [27] J. Schneider, B. Dischler, H. Seelewind, P. M. Mooney, J. Lagowski, M. Matsui, D. R. Beard, and R. C. Newman, *Appl. Phys. Lett.* **54**, 1442 (1989).
- [28] M. Skowronski, S. T. Neild, and R. E. Kremer, *Appl. Phys. Lett.* **58**, 1545 (1991).
- [29] M. Skowronski, S. T. Neild, and R. E. Kremer, *Appl. Phys. Lett.* **57**, 902 (1990).
- [30] C. Y. Song, B. Pajot, and C. Porte, *Phys. Rev. B* **41**, 12330 (1990).
- [31] H. C. Alt, *Appl. Phys. Lett.* **55**, 2736 (1989).
- [32] H. C. Alt, *Appl. Phys. Lett.* **54**, 1445 (1989).
- [33] H. C. Alt, Y. V. Gomeniuk, and U. Kretzer, *J. Appl. Phys.* **101**, 073516 (2007).
- [34] M. Linde, J.-M. Spaeth, and H. C. Alt, *Appl. Phys. Lett.* **67**, 662 (1995).
- [35] F. K. Koschnick, M. Linde, M. V. B. Pinheiro, and J.-M. Spaeth, *Phys. Rev. B* **56**, 10221 (1997).
- [36] R. Jones and S. Öberg, *Phys. Rev. Lett.* **69**, 136 (1992).
- [37] T. Mattila and R. M. Nieminen, *Phys. Rev. B* **54**, 16676 (1996).
- [38] W. Orellana and A. C. Ferraz, *Phys. Rev. B* **61**, 5326 (2000).
- [39] A. Taguchi and H. Kageshima, *Phys. Rev. B* **57**, R6779 (1998).
- [40] M. Pesola, J. von Boehm, V. Sammalkorpi, T. Mattila, and R. M. Nieminen, *Phys. Rev. B* **60**, R16267 (1999).
- [41] A. Alkauskas, J. Neugebauer, A. Pasquarello, C. G. Van de Walle *et al.*, *Advanced Calculations for Defects in Materials* (Wiley, Weinheim, 2011).
- [42] A. Alkauskas, P. Broqvist, and A. Pasquarello, *Phys. Status Solidi B* **248**, 775 (2011).
- [43] H.-P. Komsa and A. Pasquarello, *Phys. Rev. B* **84**, 075207 (2011).
- [44] C. Freysoldt, J. Neugebauer, and C. G. Van de Walle, *Phys. Rev. Lett.* **102**, 016402 (2009).
- [45] H.-P. Komsa, T. T. Rantala, and A. Pasquarello, *Phys. Rev. B* **86**, 045112 (2012).
- [46] D. Colleoni and A. Pasquarello, *Appl. Surf. Sci.* **291**, 6 (2014).
- [47] D. Colleoni and A. Pasquarello, *Appl. Phys. Lett.* **103**, 142108 (2013).
- [48] C. G. Van de Walle and J. Neugebauer, *J. Appl. Phys.* **95**, 3851 (2004).
- [49] J. P. Perdew, K. Burke, and M. Ernzerhof, *Phys. Rev. Lett.* **77**, 3865 (1996).
- [50] P. Giannozzi, S. Baroni, N. Bonini, M. Calandra, R. Car, C. Cavazzoni, D. Ceresoli, G. L. Chiarotti, M. Cococcioni, I. Dabo, A. Dal Corso, S. de Gironcoli, S. Fabris, G. Fratesi, R. Gebauer, U. Gerstmann, C. Gougousis, A. Kokalj, M. Lazzeri, L. Martin-Samos, N. Marzari, F. Mauri, R. Mazzarello, S. Paolini, A. Pasquarello, L. Paulatto, C. Sbraccia, S. Scandolo, G. Sclauzero, A. P. Seitsonen, A. Smogunov, P. Umari, and R. M. Wentzcovitch, *J. Phys.: Condens. Matter* **21**, 395502 (2009).
- [51] N. Troullier and J. L. Martins, *Phys. Rev. B* **43**, 1993 (1991).
- [52] M. Fuchs and M. Scheffler, *Comput. Phys. Commun.* **119**, 67 (1999).
- [53] F. D. Murnaghan, *Proc. Natl. Acad. Sci. USA* **30**, 244 (1944).
- [54] A. Dal Corso, A. Pasquarello, A. Baldereschi, and R. Car, *Phys. Rev. B* **53**, 1180 (1996).
- [55] I.-H. Lee and R. M. Martin, *Phys. Rev. B* **56**, 7197 (1997).
- [56] *Physics of Groups IV Elements and III-V Compounds*, New Series, Group 3, Vol. 17, edited by O. Madelung and Landolt-Börnstein (Springer, Berlin, 1982).
- [57] H. J. McSkimin, A. Jayaraman, and P. Andreatch, Jr, *J. Appl. Phys.* **38**, 2362 (1967).
- [58] *Handbook of Chemistry and Physics*, 72nd ed., Vol. 17, edited by D. R. Lide (CRC Press, Boca Raton, FL, 1991).
- [59] *Atomic Energy Levels*, 1970 ed., Vol. Circ. No. 467, edited by C. E. Moore (U. S. Natl. Bur. Standards, Washington, DC, 1970).
- [60] H. Hotop and W. C. Lineberger, *J. Phys. Chem. Ref. Data* **14**, 731 (1985).
- [61] *Molecular Spectra and Molecular Structure: IV. Constants of Diatomic Molecules*, edited by H. Huber and G. Herzberg (Van Nostrand Reinhold, New York, 1979), p. 490.
- [62] P. A. Schultz and O. A. von Lilienfeld, *Modell. Simul. Mater. Sci. Eng.* **17**, 084007 (2009).

- [63] J. Heyd, G. E. Scuseria, and M. Ernzerhof, *J. Chem. Phys.* **124**, 219906 (2006).
- [64] J. Heyd, G. E. Scuseria, and M. Ernzerhof, *J. Chem. Phys.* **118**, 8207 (2003).
- [65] H.-P. Komsa, P. Broqvist, and A. Pasquarello, *Phys. Rev. B* **81**, 205118 (2010).
- [66] I. Vurgaftman, J. R. Meyer, and L. R. Ram-Mohan, *J. Appl. Phys.* **89**, 5815 (2001).
- [67] P. Broqvist, A. Alkauskas, and A. Pasquarello, *Phys. Rev. B* **80**, 085114 (2009).
- [68] T. Todorova, A. P. Seitsonen, J. Hutter, I.-F. W. Kuo, and C. J. Mundy, *J. Phys. Chem. B* **110**, 3685 (2006).
- [69] Y. Wang, S. de Gironcoli, N. S. Hush, and J. R. Reimers, *J. Am. Chem. Soc.* **129**, 10402 (2007).
- [70] A. Alkauskas, P. Broqvist, and A. Pasquarello, *Phys. Rev. Lett.* **101**, 046405 (2008).
- [71] A. Alkauskas and A. Pasquarello, *Phys. Rev. B* **84**, 125206 (2011).
- [72] H.-P. Komsa and A. Pasquarello, *J. Phys.: Condens. Matter* **24**, 045801 (2012).
- [73] G. Pacchioni, F. Frigoli, D. Ricci, and J. A. Weil, *Phys. Rev. B* **63**, 054102 (2000).
- [74] J. Lægsgaard and K. Stokbro, *Phys. Rev. Lett.* **86**, 2834 (2001).
- [75] A. Carvalho, A. Alkauskas, A. Pasquarello, A. K. Tagantsev, and N. Setter, *Phys. Rev. B* **80**, 195205 (2009).
- [76] J. L. Lyons, A. Janotti, and C. G. Van de Walle, *Phys. Rev. Lett.* **108**, 156403 (2012).
- [77] P. Rudolph and M. Jurisch, *J. Cryst. Growth* **198**, 325 (1999).
- [78] M. Jurisch, F. Börner, T. Büinger, S. Eichler, T. Flade, U. Kretzer, A. Köhler, J. Stenzenberger, and B. Weinert, *J. Cryst. Growth* **275**, 283 (2005).
- [79] B. A. Joyce, *Rep. Prog. Phys.* **48**, 1637 (1985).
- [80] D. Schiferl and C. S. Barrett, *J. Appl. Crystallogr.* **2**, 30 (1969).
- [81] C. Hinkle, E. Vogel, P. Ye, and R. Wallace, *Curr. Opin. Solid State Mater. Sci.* **15**, 188 (2011).
- [82] S. Geller, *J. Chem. Phys.* **33**, 676 (1960).
- [83] H.-P. Komsa (private communication).
- [84] G. Makov, R. Shah, and M. C. Payne, *Phys. Rev. B* **53**, 15513 (1996).
- [85] F. El-Mellouhi and N. Mousseau, *Phys. Rev. B* **71**, 125207 (2005).
- [86] A. F. Wright and N. A. Modine, *Phys. Rev. B* **91**, 014110 (2015).
- [87] J. T. Schick, C. G. Morgan, and P. Papoulias, *Phys. Rev. B* **66**, 195302 (2002).
- [88] G. Henkelman, B. P. Uberuaga, and H. Jónsson, *J. Chem. Phys.* **113**, 9901 (2000).
- [89] J. Coutinho, R. Jones, P. R. Briddon, and S. Öberg, *Phys. Rev. B* **62**, 10824 (2000).
- [90] J. F. Binder and A. Pasquarello, *Phys. Rev. B* **89**, 245306 (2014).
- [91] J. Robertson and L. Lin, *Appl. Phys. Lett.* **99**, 222906 (2011).
- [92] N. Marzari, A. A. Mostofi, J. R. Yates, I. Souza, and D. Vanderbilt, *Rev. Mod. Phys.* **84**, 1419 (2012).
- [93] D. Colleoni, G. Miceli, and A. Pasquarello, *Phys. Rev. B* **92**, 125304 (2015).
- [94] J. Neugebauer and C. G. Van de Walle, *Mater. Res. Soc. Symp. Proc.* **395**, 645 (1996).
- [95] G. A. Baraff and M. Schlüter, *Phys. Rev. B* **33**, 7346 (1986).
- [96] D. Colleoni and A. Pasquarello, *Microelectron. Eng.* **109**, 50 (2013).
- [97] G. Hollinger, R. Skheyta-Kabbani, and M. Gendry, *Phys. Rev. B* **49**, 11159 (1994).
- [98] A. J. Bard, R. Parsons, and J. Jordan, *Standard Potentials in Aqueous Solution* (CRC Press, Boca Raton, FL, 1985).